Journal of Computational Acoustics, Vol. 16, No. 4 (2008) 563–576

INTERNATIONAL ASSOCIATION
FOR MATHEMATICS AND
COMPUTERS IN SIMULATION

A FOURTH-ORDER ACCURATE SCHEME FOR SOLVING ONE-DIMENSIONAL HIGHLY NONLINEAR STANDING WAVE EQUATION IN DIFFERENT THERMOVISCOUS FLUIDS

MAJID NABAVI*, M. H. KAMRAN SIDDIQUI and JAVAD DARGAHI

Department of Mechanical and Industrial Engineering
Concordia University, 1455 de Maisonneuve Blvd. West
Montreal, Quebec, Canada H3G 1M8
**m_nabav@encs.concordia.ca*

Received 26 September 2006
Revised 11 February 2008

Combination of a fourth-order Padé compact finite difference discretization in space and a fourth-order Runge–Kutta time stepping scheme is shown to yield an effective method for solving highly nonlinear standing waves in a thermoviscous medium. This accurate and fast-solver numerical scheme can predict the pressure, particle velocity, and density along the standing wave resonator filled with a thermoviscous fluid from linear to strongly nonlinear levels of the excitation amplitude. The stability analysis is performed to determine the stability region of the scheme. Beside the fourth-order accuracy in both time and space, another advantage of the given numerical scheme is that no additional attenuation is required to get numerical stability. As it is well known, the results show that the pressure and particle velocity waveforms for highly nonlinear waves are significantly different from that of the linear waves, in both time and space. For highly nonlinear waves, the results also indicate the presence of a wavefront that travels along the resonator with very high pressure and velocity gradients. Two gases, air and CO_2, are considered. It is observed that the slopes of the traveling velocity and pressure gradients are higher for CO_2 than those for air. For highly nonlinear waves, the results also indicate the higher asymmetry in pressure for CO_2 than that for air.

Keywords: Nonlinear standing waves; compact finite difference method; Runge–Kutta method; stability analysis.

1. Introduction

Strongly nonlinear acoustics is devoted to waves of amplitude high enough that the finite-amplitude assumption, $|\rho'| \ll \rho_0, |p'| \ll p_0$, is violated ($\rho$ and p are density and pressure, respectively, which can be written as $\rho = \rho_0 + \rho'$ and $p = p_0 + p'$, where prime denotes perturbation in the given parameter and subscript "0" represents the static value). When nonlinear terms in the conservation equations are retained, great mathematical difficulty is encountered and the analytical solution even in special cases is very difficult or nearly

*Corresponding author.

impossible. Therefore, numerical approaches are frequently used. Ilinskii *et al.*[1] developed a one-dimensional model to analyze nonlinear standing waves in an acoustical resonator. In their model, the entire resonator was driven harmonically with an acceleration of constant amplitude. They only included the attenuation associated with viscosity and solved the model equation in the frequency domain. A numerical model for nonlinear standing waves, based on a second-order wave equation written in Lagrangian coordinates, was presented by Vanhille and Campos-Pozuelo.[2] They presented a numerical formulation to model the standing acoustic wave of finite but moderate amplitude based on the finite difference method (FDM). Later, they extended their methods to two-dimensional nonlinear resonators.[3] In their model, losses due to the thermal conductivity of the fluid and walls of the tube were not taken into account. They also compared finite difference and finite volume methods (FVM) for nonlinear standing ultrasonic waves in fluid media and found reasonable agreement between the two schemes.[4] Finite element method (FEM) has been used for the study of nonlinear standing waves in rigid-walled air-filled and water-filled tubes.[5] The comparison between the results of different methods developed in these studies shows that, although FEM and FVM may have some advantages over FDM to simulate 3D nonlinear fields in irregular geometries, for simple geometries in 1D and 2D, FDM is preferred because of its lower computational cost. A study of nonlinear acoustic waves in homentropic perfect gas was presented by Christov *et al.*[6] They solved the unsteady nonlinear wave equation using a Godunov-type finite difference scheme, which is second-order accurate in space and time. They however, did not consider the effect of thermoviscous attenuation. A numerical model for quasi-standing nonlinear standing waves in a viscous fluid, based on a second-order Taylor expansion of the state equation was presented by Vanhille and Campos-Pozuelo.[7] Their second-order accurate model is valid for any viscous fluid but for a limited range of amplitudes. In a later work, they proposed a nonlinear equation based on conservation laws (written in Lagrangian coordinates) and the isentropic state equation, and numerically solved the equation using second-order accurate implicit finite difference scheme.[8] They did not impose any restriction on the nonlinearity level in the momentum equation but they used a simplified form of continuity equation which is only valid for finite-amplitude waves. Furthermore, they considered the fluid to be viscous but thermally nonconducting. Bednařík and Červenka[9] developed a model for finite-amplitude standing waves in acoustical resonators of variable cross-section. Their model takes into account external driving force, gas-dynamic nonlinearities, and thermoviscous dissipation. They solved the model numerically using central semi-discrete difference scheme developed by Kurganov and Tadmor.[10] Later, they extended their method to nonlinear standing waves in two-dimensional acoustic resonators.[11] Their model is second-order accurate in space and third-order accurate in time. They however, did not present any details about their numerical scheme.

As the literature review indicates, the accuracy of all previously developed schemes is of second-order in space and of second or third order in time. In this study, we have presented the three-dimensional exact wave equation for acoustic standing waves of arbitrary amplitude in a tube excited by a vibrating diaphragm and filled with a thermoviscous fluid. The effect of both thermoviscous attenuation and wall absorbtion have been considered

in this model. Next, we have presented a high-order numerical scheme for solving highly nonlinear standing waves equation in one-dimension with no restriction on the nonlinearity level and type of the fluid. The numerical scheme is fourth-order accurate in both time and space. Up to the knowledge of the authors, this is the first fourth-order accurate scheme reported for solving highly nonlinear standing waves.

2. High-Amplitude Nonlinear Wave Equation

The wave equation for the high-amplitude nonlinear acoustic waves in a viscous, heat-conducting fluid is derived from the basic equations of fluid mechanics (continuity and Navier–Stokes equations) along with the appropriate state equation,

$$\rho_t + \nabla(\rho \mathbf{v}) = 0, \tag{1}$$

$$\rho\left(\frac{\partial \mathbf{v}}{\partial t} + (\mathbf{v}.\nabla)\mathbf{v}\right) = -\nabla p + \left(\mu_B + \frac{4}{3}\mu\right)\nabla(\nabla \mathbf{v}), \tag{2}$$

$$p' = p_0\left(\frac{\rho}{\rho_0}\right)^{\gamma} - \kappa\left(\frac{1}{c_V} - \frac{1}{c_p}\right)\nabla \mathbf{v}, \tag{3}$$

where $\mathbf{v} = (u, v, w)$ is the acoustic velocity vector, μ and μ_B are the shear and bulk viscosities, $\gamma = c_p/c_V$ is the ratio of specific heats at constant pressure and constant volume, κ is the coefficient of thermal conduction, and t is time.

It is now useful to introduce the sound speed c as

$$c^2 = \frac{dp'}{d\rho}. \tag{4}$$

For very small perturbation ($\rho' \to 0, p' \to 0$), c becomes a constant, i.e. $c_0 = \sqrt{\gamma p_0/\rho_0}$, which is called small-signal sound speed. Using Eqs. (3) and (4) we can express ρ and p' in terms of c as[14]

$$\rho = \rho_0\left(\frac{c}{c_0}\right)^{2/(\gamma-1)}, \tag{5}$$

$$p' = p_0\left(\frac{c}{c_0}\right)^{2\gamma/(\gamma-1)}. \tag{6}$$

Now the continuity and Navier–Stokes equations can be written as

$$\frac{\partial c}{\partial t} + \mathbf{v}\nabla c + \frac{\gamma - 1}{2}c\nabla \mathbf{v} = 0, \tag{7}$$

$$\frac{\partial \mathbf{v}}{\partial t} + \mathbf{v}\nabla \mathbf{v} + \frac{2}{\gamma - 1}c\nabla c = \nu b\left(\frac{c}{c_0}\right)^{-2/(\gamma-1)}\nabla(\nabla \mathbf{v}), \tag{8}$$

where ν is the kinematic viscosity and b indicates the total effect of viscosity and thermal conductivity of the fluid as well as the wall absorbtion, and can be obtained as

$$b = \frac{2c_0^3\alpha}{\omega^2\nu}, \tag{9}$$

where $\omega = 2\pi f$, f is the frequency of excitation, and α is the total absorbtion coefficient which is the sum of thermoviscosity absorbtion coefficient and wall absorbtion coefficient.[12] We write

$$\alpha = \alpha_{tv} + \alpha_{\text{wall}},$$
$$\alpha_{tv} = \frac{\omega^2 \nu}{2c_0^3}\left(\frac{4}{3} + \frac{\mu_B}{\mu} + \frac{\gamma - 1}{P_r}\right), \quad \alpha_{\text{wall}} = \sqrt{\frac{\omega\nu}{8c_0^2}}\left(1 + \frac{\gamma - 1}{\sqrt{P_r}}\right)\frac{\wp}{\Lambda}, \tag{10}$$

where $P_r = \mu C_p/\kappa$ is called the Prandtl number, Λ is the cross-sectional area, and $\wp$ is the perimeter of the resonator.[13]

Equations (7) and (8) are the exact highly nonlinear wave equations in a thermoviscous fluid. In one dimension they can be written as

$$c_t + uc_x + \frac{\gamma - 1}{2}cu_x = 0, \tag{11}$$

$$u_t + uu_x + \frac{2}{\gamma - 1}cc_x = \nu b\left(\frac{c}{c_0}\right)^{-2/(\gamma-1)} u_{xx}. \tag{12}$$

Equations (11) and (12) may be combined in the conservative form as

$$U_t + AU_x = BU_{xx}, \tag{13}$$

where

$$U = \begin{bmatrix} c \\ u \end{bmatrix}, \qquad A = \begin{bmatrix} u & \dfrac{\gamma - 1}{2}c \\ \dfrac{2}{\gamma - 1}c & u \end{bmatrix}, B = \begin{bmatrix} 0 & 0 \\ 0 & \nu b\left(\dfrac{c}{c_0}\right)^{-2/(\gamma-1)} \end{bmatrix}.$$

This unsteady nonlinear equation must be solved using an appropriate numerical scheme. The acoustic pressure p', can be evaluated from c using Eq. (6).

The acoustical Reynolds number is defined as,

$$Re = \frac{c_0 v_0}{b\nu\omega}, \tag{14}$$

where v_0 is the characteristic velocity of the medium, $1/\omega$ is the characteristic time. Nonlinear acoustical theory must be used when the amplitude of the oscillations of the medium is sufficiently large, so that $Re \geq 1$.[14]

The fluid is assumed to be initially at rest which means particle displacement and velocity at $t = 0$ are zero. The fluid is excited by the harmonic motion of a diaphragm at $x = 0$ at the frequency f. Assuming L to be the length of the tube, the following initial and boundary

conditions for the variables u and c are applicable:

$$\begin{aligned} u(0,t) &= u_0 \sin(wt), \quad u(L,t) = 0, \\ c_x(0,t) &= 0, \quad c_x(L,t) = 0, \\ u(x,0) &= 0, \quad c(x,0) = c_0. \end{aligned} \tag{15}$$

Since the boundary condition for the density in a closed standing tube is $\rho_x = 0$ for $x = 0, L$,[9] according to Eq. (5), the appropriate boundary condition for the variable c would be $c_x = 0$ for $x = 0, L$. It must be noted that any time-dependent excitation function can be modeled using appropriate boundary conditions.

3. Numerical Analysis

The mathematical formulation outlined in Sec. 2 is solved numerically using the fourth-order compact finite difference method (CD4) in space and fourth-order Runge–Kutta time stepping scheme. Explicit finite difference schemes express the nodal derivatives as an explicit weighted sum of the nodal values of the function, whereas implicit or compact schemes (also called Padé schemes) equate a weighted sum of the nodal derivatives to a weighted sum of the nodal values of the function. Using CD4 scheme, we can express the spatial derivatives as $u'_{i+1} + 4u'_i + u'_{i-1} = 3(u_{i+1} - u_{i-1})/h$ and $u''_{i+1} + 10u''_i + u''_{i-1} = 12(u_{i+1} - 2u_i + u_{i-1})/h^2$ or as

$$\begin{aligned} (u_x)_i &= \left(1 + \frac{h^2}{6}\delta_x^2\right)^{-1} \delta_x^0 u_i + O(h^4), \\ (u_{xx})_i &= \left(1 + \frac{h^2}{12}\delta_x^2\right)^{-1} \delta_x^2 u_i + O(h^4), \end{aligned} \tag{16}$$

where $\delta_x^0 u_i = (u_{i+1} - u_{i-1})/2h$, $\delta_x^2 u_i = (u_{i+1} - 2u_i + u_{i-1})/h^2$, $h = \Delta x$, and $u_i = u(x_i)$. With the same stencil width, compact schemes are more accurate than explicit ones.[15]

For the time evolution equation,

$$\frac{\partial U}{\partial t} = F(U), \tag{17}$$

where

$$F(U) = -AU_x + BU_{xx}, \tag{18}$$

an explicit, p-stage Runge–Kutta scheme advances the solution from time level $t = t_n$ to $t_n + \tau$ as

$$U^{n+1} = U^n + \sum_{i=1}^{p} \zeta_i R_i, \tag{19}$$

where

$$R_1 = \tau F(U^n), \quad R_i = \tau F(U^n + \sigma_{i-1} R_{i-1}). \tag{20}$$

For four-stage Runge–Kutta scheme, we have $\zeta = [1/6, 1/3, 1/3, 1/6]$ and $\sigma = [1/2, 1/2, 1]$.

3.1. *Discretization of the nonlinear wave equation*

Using Eqs. (16) and (18) we can write

$$\left(1+\frac{h^2}{6}\delta_x^2\right)\left(1+\frac{h^2}{12}\delta_x^2\right)F_i = -A_i\left(1+\frac{h^2}{12}\delta_x^2\right)\delta_x^0 U_i + B_i\left(1+\frac{h^2}{6}\delta_x^2\right)\delta_x^2 U_i. \tag{21}$$

Obviously, the stencil on the left-hand side of Eq. (21) is five-node and requires to solve the system of equations with penta-diagonal coefficient matrix. The reason for the increased stencil is that the denominators of the Padé approximation for U_x and U_{xx} (Eq. (16)) are not equal. In order to obtain small-stencil with the same fourth-order accuracy, we follow the approach of Lele[15] and write

$$(u_{xx})_i = \left(1+\frac{h^2}{6}\delta_x^2\right)^{-1}\left(\frac{1}{3}\hat{\delta}_x^2+\frac{2}{3}\delta_x^2\right)u_i + O(h^4), \tag{22}$$

where $\hat{\delta}_x^2 u_i = (u_{i+2} - 2u_i + u_{i-2})/h^2$. Using Eq. (22), Eq. (18) can be discretized as

$$\left(1+\frac{h^2}{6}\delta_x^2\right)F_i = -A_i\delta_x^0 U_i + \frac{1}{3}B_i(\hat{\delta}_x^2+2\delta_x^2)U_i. \tag{23}$$

This is a tridiagonal system which can be solved efficiently using fourth-order Runge–Kutta time-stepping scheme. Since tridiagonal matrices can be inverted quite efficiently, this method is very attractive and efficient. This invertibility also proves the solvability of Eq. (23).

3.2. *Stability analysis*

The choice of the time step τ is an important issue in solving unsteady equations. One criterion for the time step is that the time integration must be stable. Following Jameson *et al.*[16], the amplification factor of the four-step Runge–Kutta method is given as

$$\xi = 1 + Z + \frac{Z^2}{2} + \frac{Z^3}{6} + \frac{Z^4}{24}, \tag{24}$$

where Z is the Fourier symbol of the discretized $F(U)$ (Eq. (18)). Applying von Neumann stability analysis method[17] to Eq. (23) we can obtain

$$Z = \frac{r(4\cos(\beta)+2\cos(2\beta)-6) - 3\sqrt{-1}s\sin(\beta)}{\cos(\beta)+2}, \tag{25}$$

where $s = \lambda_A\tau/h$ and $r = \lambda_B\tau/h^2$, λ_A and λ_B are the eigenvalues of matrices A and B which can be obtained as $\lambda_A = v \pm c$ and $\lambda_B = \nu b(c/c_0)^{-2/(\gamma-1)}$, $\beta = 2\pi mh/L, m = 0, 1, \ldots, N$,

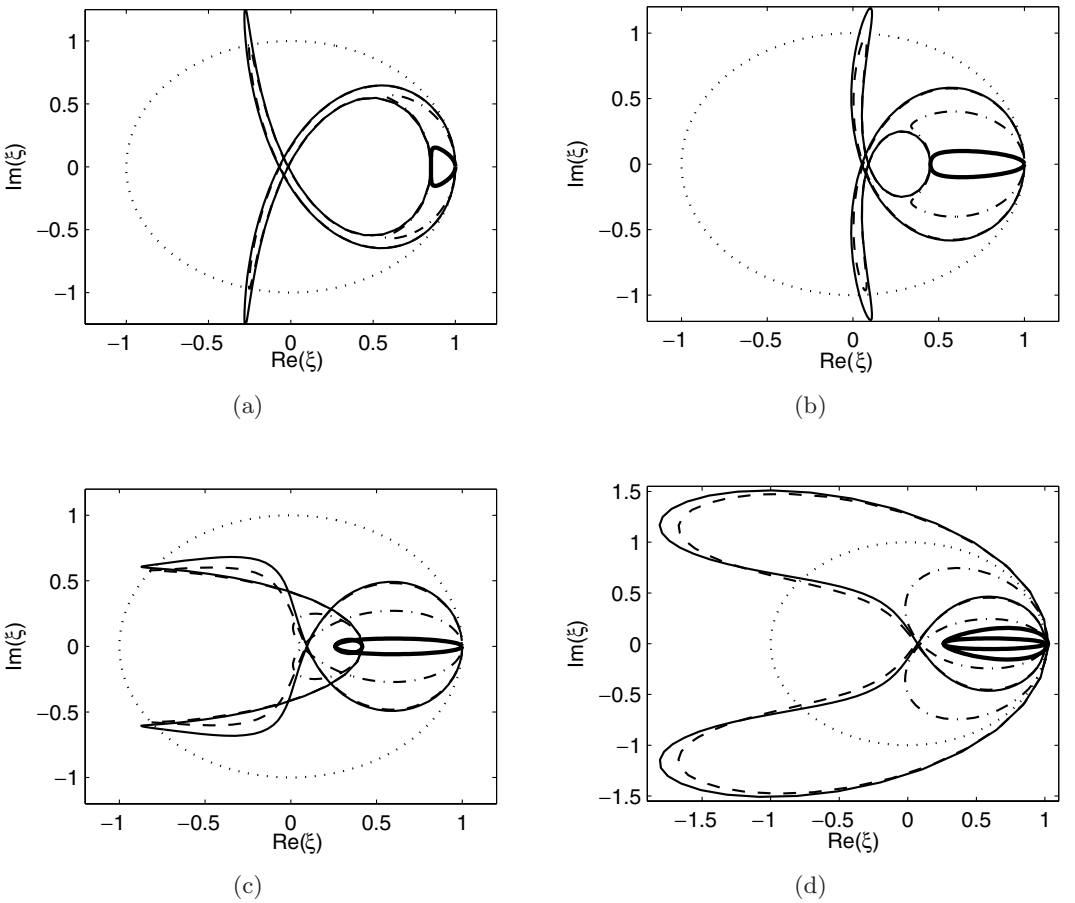

Fig. 1. The stability footprints of the given scheme for $s = 0.1$ (thick-solid); 0.5 (thin dash-dotted), 1.2 (thin dashed), and 1.25 (thin solid) and different values of r (a) $r = 0.02$, (b) $r = 0.1$, (c) $r = 0.274$, and (d) $r = 0.35$; dot line is $|\xi| = 1$ circle.

and N is the number of nodes in the x-direction. Applying von Neumann stability method to large-stencil scheme (Eq. (21)) will result in

$$Z = \frac{12r(\cos(2\beta) + 2\cos(\beta) - 3) - 15\sqrt{-1}s(\sin(2\beta) + 2\sin(\beta))}{\cos(2\beta) + 14\cos(\beta) + 21}. \tag{26}$$

The magnitude of the amplification factor is related to the artificial dissipation. When $|\xi| \geq 1$, the method is unstable. For unsteady cases, we like $|\xi|$ to be as close as possible to unity to ensure stability with minimum artificial dissipation.

The stability footprints (imaginary part of ξ versus its real part) of the small-stencil scheme (Eq. (23)) for different values of s and r are depicted in Fig. 1. The stability region of the given scheme is: $s \leq 1.2$ and $r \leq 0.274$. Figure 1(a) shows that, to get $|\xi|$ as close as possible to unity, we need smaller values for s and r, which means that we must increase the node numbers in both x and t directions. As seen in Figs. 1(a)–1(c), for $s > 1.2$ regardless the value of r, the scheme is unstable. Figure 1(d) shows that for $r > 0.35$ regardless the

value of s, the scheme is unstable. The stability footprint for the marginal values of s and r ($s = 1.2$ and $r = 0.274$) is included in Fig. 1(c). The stability region of the large-stencil scheme (Eq. (21)) is: $s \leq 1.345$ and $r \leq 0.46$.

4. Results and Discussion

Numerical calculations were performed using the small-stencil scheme (Eq. (23)) for two thermoviscous gases, air and CO_2 at 0°C. For both cases, the cross-sectional area of the resonator is set equal to 16 cm^2, the excitation frequency is 1024 Hz, and the length of the resonator is set equal to half of the wavelength of the acoustic standing wave, which is equal to 16.2 cm for air and 12.6 cm for CO_2. The values of physical parameters of these gases for the given conditions are presented in Table 1. Also presented in Table 1 are the values of the absorbtion coefficient and corresponding values of b, computed from Eqs. (9) and (10). The values of μ_B/μ have been obtained from Pan *et al.*[18]

For numerical simulations, the spatial and temporal step sizes were set as $h = 0.81$ mm and $\tau = 0.244\,\mu$s, respectively, The corresponding values of s and r are 0.121 and 0.098, respectively, which satisfy the stability condition with low artificial dissipation. One advantage of the given numerical scheme is that no additional attenuation is required to get numerical stability.

Figure 2 represents the variation of the pressure and particle velocity over one standing wave period for air. Figure 2(a) shows that in the highly nonlinear standing wave case, the pressure waveform distorts from the pure sinusoidal waveform which is observed in the linear case. Figure 2(b) shows that nonlinearity significantly influences the particle velocity profile. The particle velocity waveform is also deviated from the sinusoidal behavior. For the linear case, the velocity profile is symmetric about the pressure node (i.e. at $L/2$). However, for the highly nonlinear case, the plot shows a steep wavefront traveling along the resonator.

To get a better insight into the pressure and velocity dynamics of highly nonlinear waves, the pressure waveform at $x = L$ (i.e. pressure antinode) and particle velocity waveform at $x = L/2$ (i.e. velocity antinode) are plotted in Figs. 3(a) and 3(b), respectively, for air and CO_2. The maximum velocity of the diaphragm for both cases is $u_0 = 10$ (m/s) that

Table 1. Values of parameters for air and CO_2 at 0°C.

	Air	CO_2
μ (kg/ms)	0.0000181	0.0000145
μ_B/μ	0.6	1000
ρ_0 (kg/m^3)	1.293	1.98
c_0 (m/s)	331.6	258
γ	1.402	1.289
κ (J/Kms)	0.026	0.017
c_p (J/kgK)	1005	846
α (m^{-1})	0.1196	0.0916
b	15050	10373

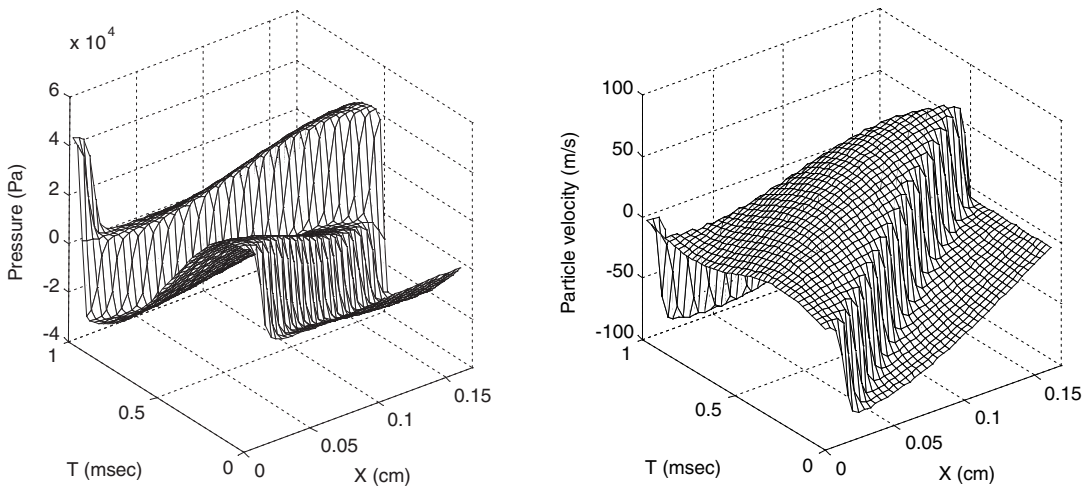

Fig. 2. (a) Pressure and (b) particle velocity over a standing wave period for air. Maximum velocity of the diaphragm is $u_0 = 10$ (m/s).

corresponds to the acoustical Reynolds number (Eq. (14)) of 14.23 and 27.45 for air and CO_2, respectively. The plots show that the shape of pressure and velocity waveforms for both gases are similar. However, for air, the pressure amplitude is lower and the particle velocity amplitude is higher than that for CO_2. This is due to the reason that the absorbtion coefficient of CO_2 for the given frequency and other conditions is less than that of air, resulting in higher pressure amplitude.

Figure 3(a) also shows another important difference between the temporal pressure waveforms for air and CO_2. The asymmetry of the pressure wave for CO_2 is higher than that for air. This phenomenon can be explained using the Re. Due to lower values of b and ν for CO_2 than those for air, Re is higher for CO_2 than that for air. The higher value of Re for CO_2 means that the degree of nonlinearity is higher for CO_2 than that for air. As the degree of nonlinearity increases, more energy will transfer to distortion components of the wave[1,19]. Table 2 shows the relative harmonic amplitudes ($p_n/p_1; n = 0, 2, 3, 4$) of the pressure waveforms for air and CO_2, where p_1 is the amplitude of the fundamental frequency. The relative amplitude of the dc component (p_0) is higher for CO_2 than that for air. The higher dc pressure gives the upward shift in the pressure waveform and is responsible for the higher asymmetry in the pressure wave for CO_2.

To study the influence of nonlinearity on the pressure and particle velocity, the pressure variations at $x = L$ and particle velocity variations at $x = L/2$ from the center of the diaphragm over two standing wave periods for $u_0 = 0.1, 0.5, 1$, and 5 (m/s) are depicted in Fig. 4 for air. The corresponding values of the acoustical Reynolds numbers for the given cases are $1.04, 3.05, 4.4, 6.3$ and 10.04. These cases cover a range from linear to highly nonlinear standing waves. Figure 4(a) shows that the shape of pressure waveform changes from sinusoidal in the linear case to saw-tooth in the highly nonlinear case. The plot also shows

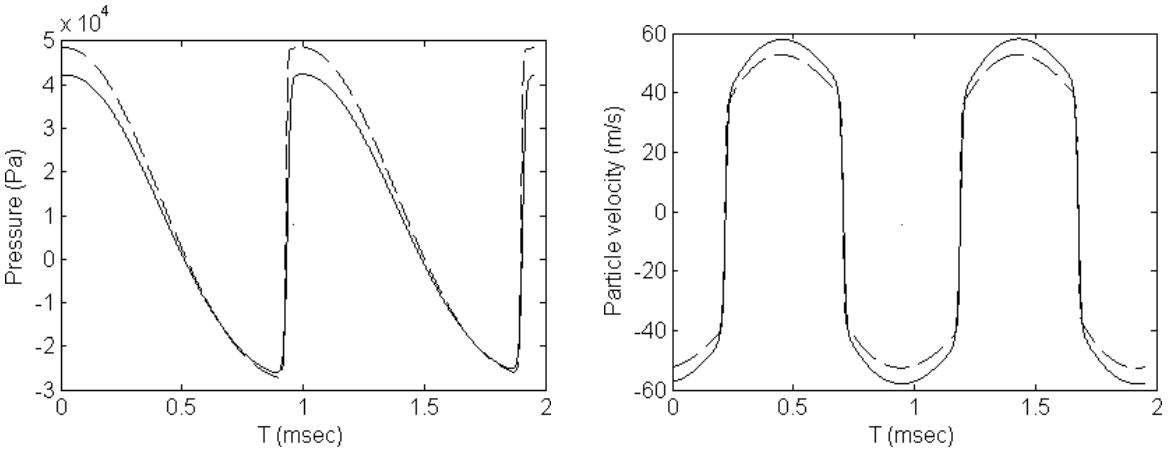

(a) (b)

Fig. 3. (a) Pressure waveform at $x = L$ and (b) particle velocity waveform at $x = L/2$ from the center of the diaphragm over two standing wave periods for air (solid line) and CO_2 (dashed line). Maximum velocity of the diaphragm is $u_0 = 10$ (m/s).

Table 2. Relative harmonic amplitudes of the pressure waveforms (p_n/p_1) for air and CO_2.

Harmonic	Air	CO_2
dc	0.56	0.67
2	0.36	0.40
3	0.24	0.26
4	0.17	0.19

that as the nonlinearity effect increases, the pressure waveform becomes asymmetric about the static pressure, and the pressure peaks shift toward the pressure antinodes. The shift in the pressure peaks is due to the increase in the amplitudes of second and higher harmonics with nonlinearity. Figure 4(b) shows that as the nonlinearity increases, high velocity gradients are observed around $T/4$ and $3T/4$ and the waveform changes to near-rectangular form. Similar waveforms for pressure and particle velocity are reported by Bednařík and Červenka.[9] However, for their simulations, the acoustical Reynolds number was around 4, which is in the moderate nonlinearity range.

Figure 2 shows that nonlinearity influences the spatial waveforms of pressure and particle velocity. To analyze this impact, the pressure and particle velocity waveforms along the resonator are plotted for the highly nonlinear ($u_0 = 10\,\mathrm{m/s}$) case in Figs. 5(a) and 5(b), respectively. The waveforms in this figure are plotted with a time step of $T/8$, and cover a total of half-wave period. The axial distribution of pressure shows that in the highly nonlinear case, the pressure node is not fixed in time and space. That is, during a wave period, the pressure node oscillates about the theoretical pressure node, whereas, in the

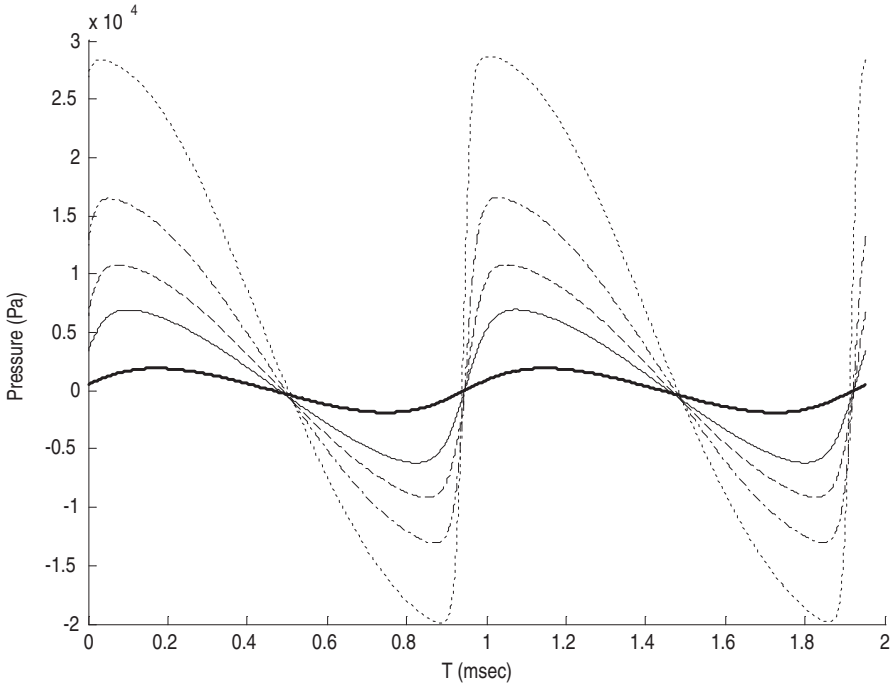

(a)

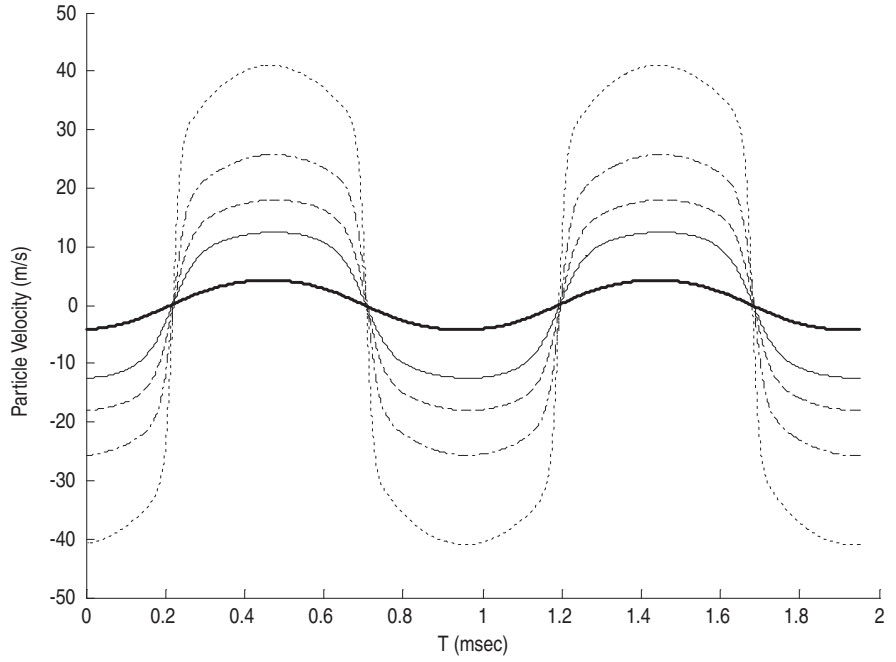

(b)

Fig. 4. (a) Pressure waveforms at $x = L$ and (b) particle velocity waveforms at $x = L/2$ from the center of the diaphragm for air for $u_0 = 0.1\,\mathrm{m/s}$ (thick solid); $u_0 = 0.5\,\mathrm{m/s}$ (thin solid); $u_0 = 1.0\,\mathrm{m/s}$ (dashed); $u_0 = 2.0\,\mathrm{m/s}$ (dash-dotted), and $u_0 = 5.0\,\mathrm{m/s}$ (dotted).

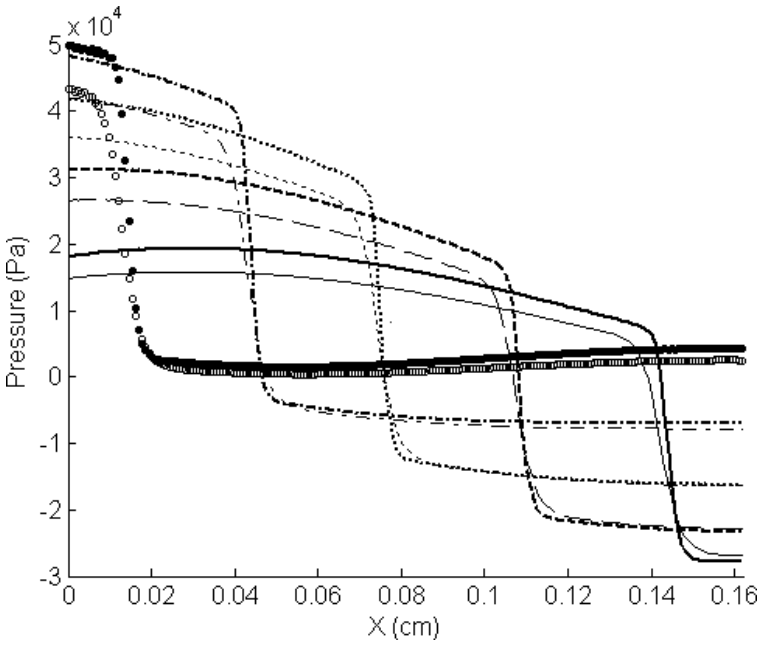

(a)

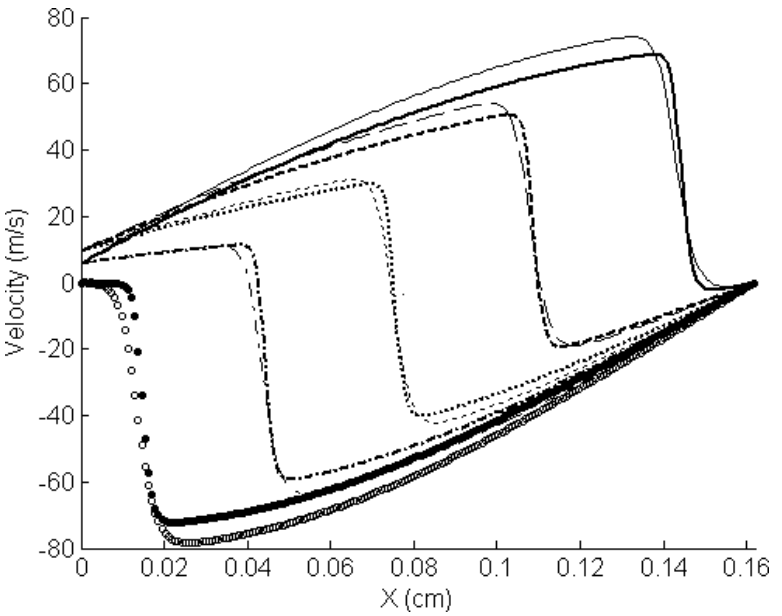

(b)

Fig. 5. Axial distributions of the (a) pressure and (b) particle velocity for both air (thin) and CO_2 (thick) for $u_0 = 10$ (m/s) at different times; $t = 0$, $\circ$; $t = T/8$ (dash-dotted); $t = T/4$ (dotted); $t = 3T/8$ (dashed), and $t = T/2$ (solid).

linear case a pressure node is present in the middle of the resonator that is fixed in time and space. In case of particle velocity, the nodes are fixed at both ends of the resonator, and the plots show that for the highly nonlinear case, the velocity peaks move across the resonator with time, whereas they are almost fixed at the middle of the resonator in the linear case. The plot in Fig. 5(b) also indicates the presence of an additional node inside the resonator whose position changes with time. The plot also shows a wavefront with high velocity gradient, which also correspond to the high pressure gradient. The ratio between the positive and negative peaks of the wavefront changes with propagation. Such wavefront is not observed in the linear case. Thus, it can be concluded that for highly nonlinear standing waves, a wavefront with very high velocity and pressure gradients travels along the resonator.

Figure 5 also shows the effect of the filled gas on the spacial pressure and particle velocity waveforms. The slopes of the traveling velocity and pressure gradients are higher for CO_2 than those for air. It means that the shock waves generated in the resonator are more intense for CO_2 compared to air, which is due to higher level of nonlinearity for CO_2.

5. Conclusions

A set of two nonlinear equations for highly nonlinear standing waves in a thermoviscous fluid is derived from the basic equations of fluid mechanics along with the appropriate state equation. The set of equations is solved numerically using the combination of a fourth-order compact finite difference scheme and a fourth-order Runge–Kutta time-stepping scheme. The result is an accurate and fast-solver numerical model which can predict the pressure, particle velocity, and density along the highly nonlinear standing wave resonator filled with a thermoviscous fluid with no restriction on nonlinearity level and type of the fluid. As it is well known, the results show that the pressure and particle velocity waveforms for highly nonlinear waves are significantly different from that of the linear waves, in both time and space. As the waves become highly nonlinear, the pressure waveform changes from sinusoidal to saw-tooth form and the particle velocity waveform changes from sinusoidal to near-rectangular form. For highly nonlinear waves, the results also indicate the presence of a wavefront that travels along the resonator with very high pressure and velocity gradients. The slopes of the traveling velocity and pressure gradients are higher for CO_2 than those for air. Another important observation is that the asymmetry in pressure waveform for CO_2 is higher than that for air.

Acknowledgments

This research is funded by the grants from Natural Science and Engineering Research Council of Canada (NSERC) and Concordia University.

References

1. Y. A. Ilinskii, B. Lipkens, T. S. Lucas and T. W. Van Doren, Nonlinear standing waves in an acoustical resonator, *J. Acoust. Soc. Am.* **104** (1998) 2664–2674.

2. C. Vanhille and C. Campos-Pozuelo, A high-order finite difference algorithm for the analysis of standing acoustic waves with finite but moderate amplitude, *J. Computat. Phys.* **165** (2000) 334–353.
3. C. Vanhille and C. Campos-Pozuelo, Numerical simulation of two-dimensional nonlinear standing waves, *J. Acoust. Soc. Am.* **116** (2004) 194–200.
4. C. Vanhille and C. Campos-Pozuelo, Finite difference and finite volume methods for nonlinear standing waves in fluid media, *Ultrasonics* **42** (2004) 315–318.
5. L. Elvira-Segura and Riera-Franco de Sarabia, A finite element algorithm for the study of nonlinear standing waves, *J. Acoust. Soc. Am.* **103** (1998) 2312–2320.
6. I. Christov, P. M. Jordan and C. I. Christov, Nonlinear acoustic propagation in homentropic perfect gases: A numerical study, *Phys. Lett. A* **353** (2006) 273–280.
7. C. Vanhille and C. Campos-Pozuelo, Three time-domain computational models for quasi-standing nonlinear acoustic waves, including heat production, *J. Computat. Acoust.* **14** (2006) 143–156.
8. C. Vanhille and C. Campos-Pozuelo, Nonlinear ultrasonic resonators: A numerical analysis in the time domain, *Ultrasonics* **44** (2006) 777–781.
9. M. Bednařík and M. Červenka, Description of finite-amplitude standing acoustic waves using convection-diffusion equations, *Czech. J. Phys.* **55** (2005) 673–680.
10. A. Kurganov and E. Tadmor, New high-resolution central schemes for nonlinear conservation laws and convection-diffusion equations, *J. Computat. Phys.* **160** (2000) 241–282.
11. M. Bednařík and M. Červenka, Nonlinear standing wave in 2D acoustic resonators, *Ultrasonics* **44** (2006) 773–776.
12. M. F. Hamilton and D. T. Blackstock, *Nonlinear Acoustics* (Academic Press, New York, 1998).
13. A. D. Pierce, *Acoustics* (Acoustical Society of America, 1989).
14. B. O. Enflo and C. M. Hedberg, *Theory of Nonlinear Acoustics in Fluids* (Kluwer Academic Publishers, 2002).
15. S. K. Lele, Compact finite difference schemes with spectral-like resolution, *J. Computat. Phys.* **103** (1992) 16–42.
16. A. Jameson, W. Schmidt and E. Turkel, Numerical solution of the Euler equations by finite volume methods using Runge–Kutta time stepping schemes, *Am. Instit. Aeronautics Astronautics* Paper 81-1259 (1981).
17. J. C. Tannehill, A. A. Anderson and R. H. Pletcher, *Computational Fluid Mechanics and Heat Transfer*, 2nd ed. (Taylor and Francis, 1997).
18. X. Pan, M. N. Shneider, Z. Zhang and R. B. Miles, Bulk viscosity measurements using coherent Rayleigh–Brillouin, in *The 42nd Aerospace Sci. Meeting Exhibit Conf. AIAA* (2004).
19. Y. A. Ilinskii, B. Lipkens and E. A. Zabolotskaya, Energy losses in an acoustical resonator, *J. Acoust. Soc. Am.* **109** (2001) 1859–1870.